

PROCEEDINGS OF SPIE

[SPIDigitalLibrary.org/conference-proceedings-of-spie](https://spiedigitallibrary.org/conference-proceedings-of-spie)

Studies of spatial uniformity and jitter in SiC UV SPADs

Anand Sampath, Gregory Garrett, Jonathan Schuster,
Jeremy Smith, Michael Derenge, et al.

Anand V. Sampath, Gregory A. Garrett, Jonathan Schuster, Jeremy L. Smith, Michael A. Derenge, Daniel B. Habersat, Brenda VanMil, Reza Gandhi, Sergei Dolinsky, Edwin J. Heilweil, Joshua C. Bienfang, Enrico Bellotti, Michael Wraback, "Studies of spatial uniformity and jitter in SiC UV SPADs," Proc. SPIE 12512, Advanced Photon Counting Techniques XVII, 1251206 (15 June 2023); doi: 10.1117/12.2663387

SPIE.

Event: SPIE Defense + Commercial Sensing, 2023, Orlando, Florida, United States

Studies of spatial uniformity and jitter in SiC UV SPADs

Anand V. Sampath*^a, Gregory A. Garrett^a, Jonathan Schuster^a, Jeremy L. Smith^a, Michael A. Derenge^a, Daniel B. Habersat^a, Brenda VanMil^a, Reza Ghandi^b, Sergei Dolinsky^b, Edwin J. Heilweil^c, Joshua C. Bienfang^c, Enrico Bellotti^d, Michael Wraback^a

^aDEVCOM Army Research Laboratory, 2800 Powder Mill Road, Adelphi, MD, USA 20783; ^bGE Research Center, Niskayuna, NY, USA 12309; ^cNational Institute of Standards and Technology, Gaithersburg, MD, USA 20878; ^dBoston University, Boston, MA, USA 02215

ABSTRACT

Ultraviolet single-photon avalanche detectors (UV-SPADs) that are low cost, size, weight, and power as well as resilient to shock, high temperatures and stray magnetic fields have a number of applications. SiC is attractive for UV SPADs as it is inherently blind to visible light, and Geiger mode as well as high-gain linear-mode devices have been demonstrated. However, issues remain regarding bias dependence of spatial uniformity of detection efficiency (DE) and responsivity as well as the temporal resolution, or jitter, in Geiger mode. Over a wide range of device structures (p- vs. n- illuminated) we observe a non-uniform responsivity across the active area for values of gain from 100 to 10^5 , and we observe that the non-uniformity is somewhat reduced at higher gain. The spatial dependence of the DE in Geiger mode agrees with linear-mode results for gain $>10^5$. This presents in all devices as an “optically dead” region on one side of the detector whose extent varies with operating conditions and is independent of contact geometry and device layout. The temporal resolution of single-photon detection is characterized with a femtosecond-pulsed source at 267 nm and found to have a full-width-at-half-maximum jitter < 92 ps, which is significantly lower than previously reported results and likely an upper bound due to the quenching circuit and the spatial non-uniformity. Numerical modeling suggests that small variations in doping densities and thicknesses of epitaxial layers might be a cause of the non-uniformity. Results also indicate that detector layer design, size, and geometry can mitigate the effects of spatial non-uniformity,

Keywords: ultraviolet avalanche photodiodes, spatial uniformity, jitter, Geiger-mode, single-photon avalanche diode, single-photon detection

1. INTRODUCTION

Currently, detectors for single-photon sensing in the ultraviolet (UV) are limited to intensified charge coupled device (iCCD) and photomultiplier tubes (PMT), as well as, for some cases, back-illuminated SiC CMOS sensors [1-3]. PMTs and iCCDs employ a photocathode to convert incident photons into electrons that are directed toward a multichannel plate array and then amplified. The detection efficiency (DE) of the detector is generally limited by the likelihood that an incident photon ejects an electron from the photocathode, the quantum efficiency (QE), which can be as high as $\approx 22\%$. However, these devices have the disadvantage of being fragile and highly susceptible to external magnetic fields. They also tend to exhibit a spectrally broadband response, which can make them unsuitable for staring applications. Similarly, while back-illuminated SiC CMOS sensors can have very low read-out noise, the DE of these devices is limited to the UV-A spectrum.

The 4H polytype of SiC is an attractive material for UV avalanche photodiodes (UV APDs), as it is both inherently blind to visible photons due to its indirect bandgap at ≈ 3.2 eV, and 150 mm diameter substrates with dislocation density below 10^4 cm⁻² are commercially available. This implies that large-area devices are practical, as the average dislocation spacing is ≈ 75 μ m. State-of-the-art SiC APDs have exhibited both high UV-C (< 280 nm) responsivity [4-6] and high multiplication gain (M) with low dark-current density (0.75 nA/cm² $< J_{\text{dark}} < 63$ nA/cm² at $M = 1000$ [7-9]) and peak multiplication gain $> 10^6$ [5,8,10]. Zhou *et al.* have reported large-area 800 μ m diameter SiC APDs with relatively low dark currents and high QE [5]. In addition, 30% single-photon detection efficiency (SPDE) with dark count probability of 8×10^{-4} per gate in gated testing has been reported for 180 μ m diameter devices that employ a recessed window [9]. Moreover, 4H-SiC solid-state photomultipliers, which are arrays of individually quenched APDs with separate absorption, charge, and multiplication regions (SACM-APDs), with detection area ≈ 4 mm² and pixel count > 1000 have been reported [11]. Lastly, a 120 μ m diameter 4H-SiC APD with a dark current of ≈ 4 nA to 60 nA at $M = 4 \times 10^5$ and SPDE of $\approx 10\%$ to 20% at 280 nm has become commercially available. Relatively less work has been done characterizing jitter in SiC

APDs; two studies report values for the FWHM of the temporal response of 650 ps, and <1 ns, for a p+:p-i-n-diode, and SACM structure, respectively [12,13].

A challenge recently identified for these devices is the spatial non-uniformity of these detectors operating in Geiger-mode. Specifically, Cai *et al.* observed that the Geiger-mode spatial non-uniformity of SiC APDs in which light entered through the p-doped side of the diode was highly dependent upon applied excess bias [14]. At low bias, these devices had large optically dead zones, where the photo-counts were not discernable from dark counts, while two hot-spots located on one side of the mesa were responsible for the detector’s photo-response. Increasing excess bias was found to improve detector spatial uniformity, nearly eliminating the optically dead zone. This behavior was attributed to non-uniformity in the breakdown electric field strength in the APD arising from either (or potentially both) the non-uniformity in the beveled mesa angle, or the difference in impact ionization along the <0001> and <11-20> directions combined with the 4° miscut of the epitaxial wafer. Previously, Guo *et al.* examined the low-gain uniformity of the spectral response in p-illuminated SiC APD structures and observed increasing spatial non-uniformity as gain increased from 100 to 10000 in their devices [15]. At higher gains, peak response was observed along one side of the circumference of their devices. This non-uniformity was attributed to small (< 1%) spatial variations of doping concentration in the highly doped contact layers of the devices fabricated across their 76.2 mm wafer. They proposed that this variation gives rise to small changes in the depletion width under high reverse bias, resulting in a meaningful reduction of the electric field, and therefore gain, across their devices.

In this paper, we report studies of the spatial uniformity of SiC APDs in linear-mode and Geiger-mode operation. We examine the effects of device geometry on the spatial uniformity and employ numerical modeling to examine possible causes of the variations observed. Lastly, jitter measurements in Geiger-mode devices are reported and discussed in the context of the spatial uniformity measurements and passive quenching.

2. EXPERIMENTAL METHODS

The 4H-SiC avalanche photodiode structures investigated consist of p-illuminated p-i-n diodes and n-illuminated separate absorption and multiplication diodes with structures similar to those previously reported [6,11]. The apparatus for making spatially dependent responsivity and single-photon detection efficiency measurements consists of a Picoquant¹ pulsed LED source emitting at 285 nm and focused to spot size of ≈ 9 μm using a combination of a lens and a reflective microscope

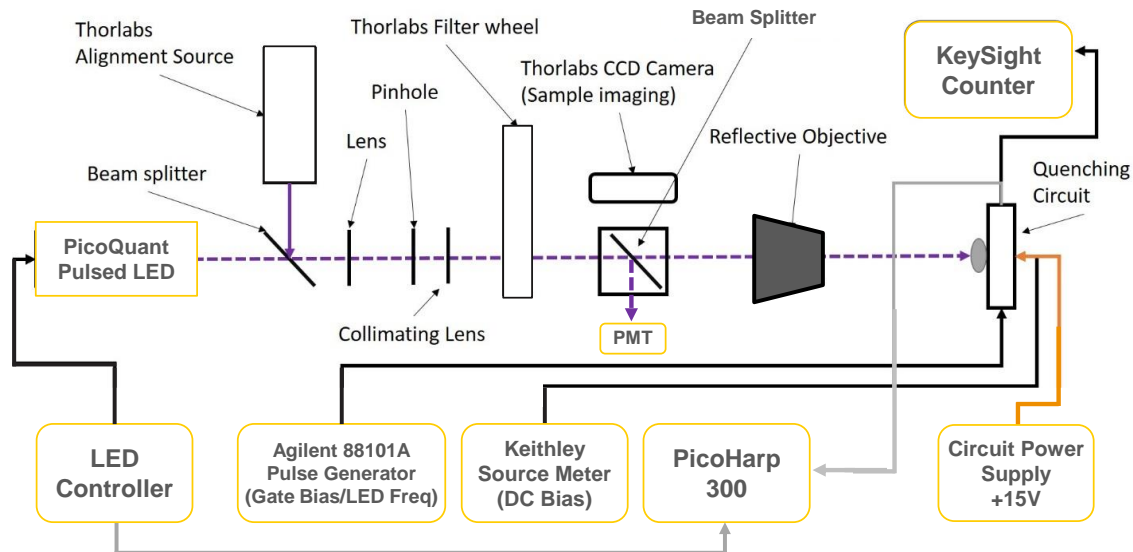


Figure 1. Scanning Single Photon Detection Efficiency/ Responsivity Setup

¹ The identification of any commercial product or trade name does not imply endorsement or recommendation by the National Institute of Standards and Technology.

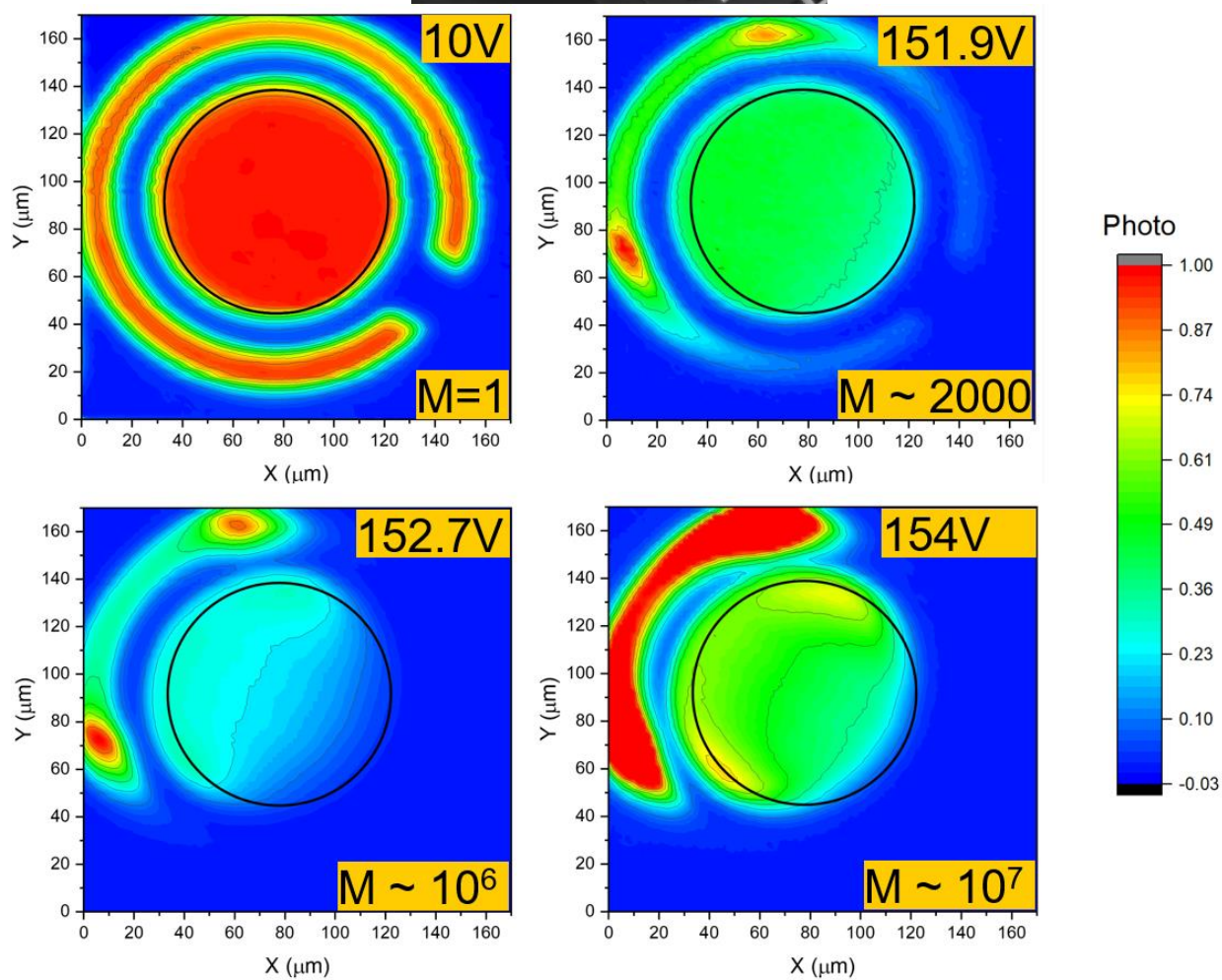


Figure 2. Optical microscope image (top) and linear-mode spatial response measurement of p-i-n SiC APD (bottom) at various levels of multiplier gain (M). Black circle identifies the photosensitive area of the APD at unity-gain.

objective, as shown in Figure 1 [16]. The pulse rate of the LED source was held at 1 MHz using a pulse generator. Responsivity measurements were made using a voltage source meter to apply DC bias and an electrometer to measure photocurrent. Single-photon detection efficiency measurements were made using a passive-quenching circuit with a 100 kΩ quench resistor and a fast comparator. The photon flux was limited to a mean of 0.05 photons per pulse to ensure accurate counting statistics in the single-photon regime [9]. Spatial maps of the responsivity and DE were made by mounting the diode test circuit to an X-Y translation stage with 2 μm step size. Measurements were made reversing the direction of the scan in the Y-direction for a number of devices to ensure that results are invariant to the measurement method.

3. SPATIAL UNIFORMITY RESULTS

The spatial dependence of the linear-mode response mesa of a 4H SiC p-illuminated p-i-n avalanche photodiode is shown in Figure 2 (bottom). The photocurrent plotted at each bias is normalized to the peak current measured for that can. For clarity, an optical microscope image of a typical device showing the location of the top-contact ring on the mesa is also shown. The response for a 100 μm diameter diode is quite uniform at low bias up to 144 V, corresponding to approximately unity gain as shown in Figure 2 bottom. The top contact ring inset within the mesa appears as an optically dead region due to absorption from the contact. The drop in photocurrent apparent near the contact ring and device mesa are attributed to the ≈ 9 μm diameter spot size of the illuminating beam and 2 μm step size of the scan that blurs out features as only a fraction of the spot is on the photosensitive portion of the mesa in this region of scan. With increasing bias and the onset of gain, the response becomes limited to one side of the mesa, with the optically dead zone expanding further along the right-side of the scan and clear hotspots developing at the top and left edges of the left side with increasing gain from 10³ to 10⁶, consistent with the results of Guo *et al.* [15]. However, an increase in the spatial uniformity is observed at the highest bias examined, a gain of ≈ 10⁷, which is similar to the results of Cai *et al.* [14]. Studies of spatial uniformity in the same device operating in Geiger mode are shown in Figure 3. Under these conditions, the device exhibits

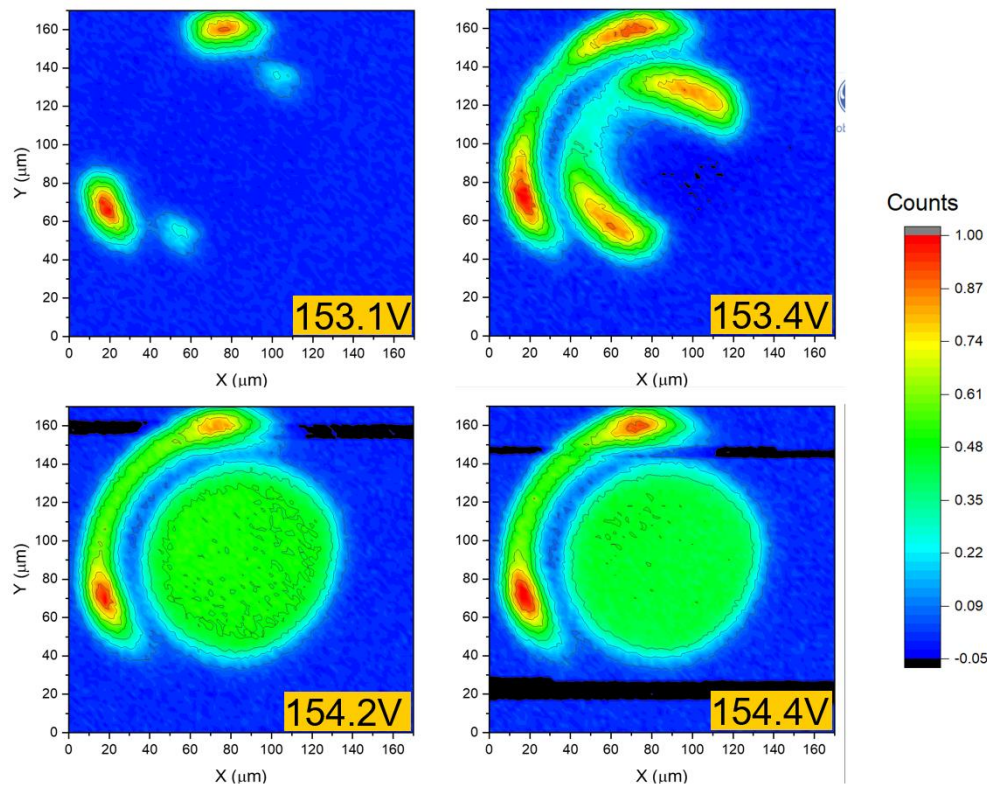


Figure 3. Spatial mapping of photoresponse and detection efficiency for various n-illuminated and p-illuminated SiC APDs

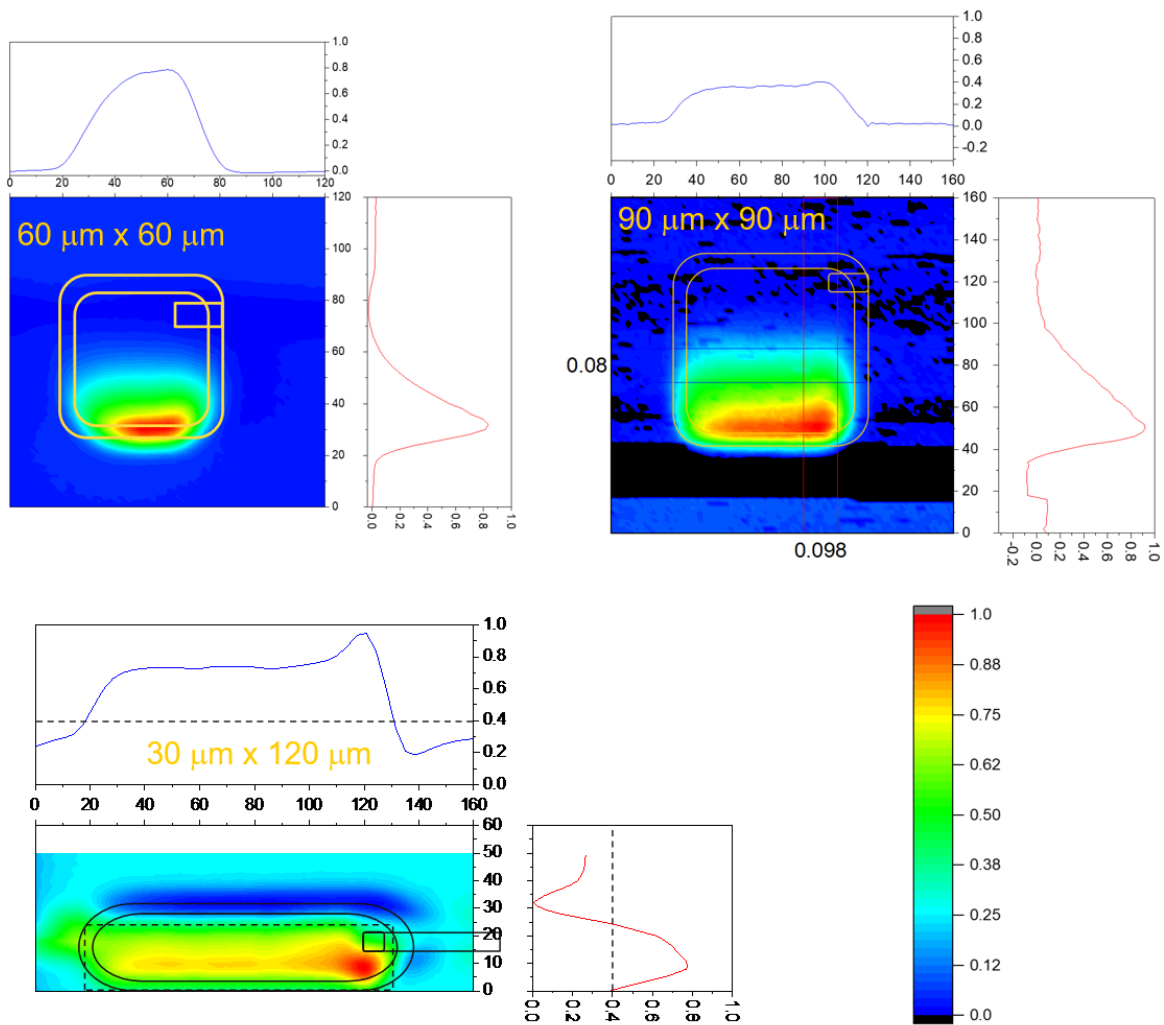


Figure 4. Spatial uniformity maps of SiC APDs at $M_{\text{peak}} = 9000$ to 15000 , with device dimensions of $60 \times 60 \mu\text{m}$, $90 \times 90 \mu\text{m}$ and $30 \times 120 \mu\text{m}$.

photo-counts above the dark count rate in only two localized hotspots at the lowest bias of 153.1 V . These hotspot locations are qualitatively similar to those observed in linear-mode operation at lower gain. Increasing the operating voltage reduces the size of the optically dead zone and improves spatial uniformity. At the highest bias investigated, 154.4 V , the spatial map becomes noisier due to the increased dark-count rate in the detector.

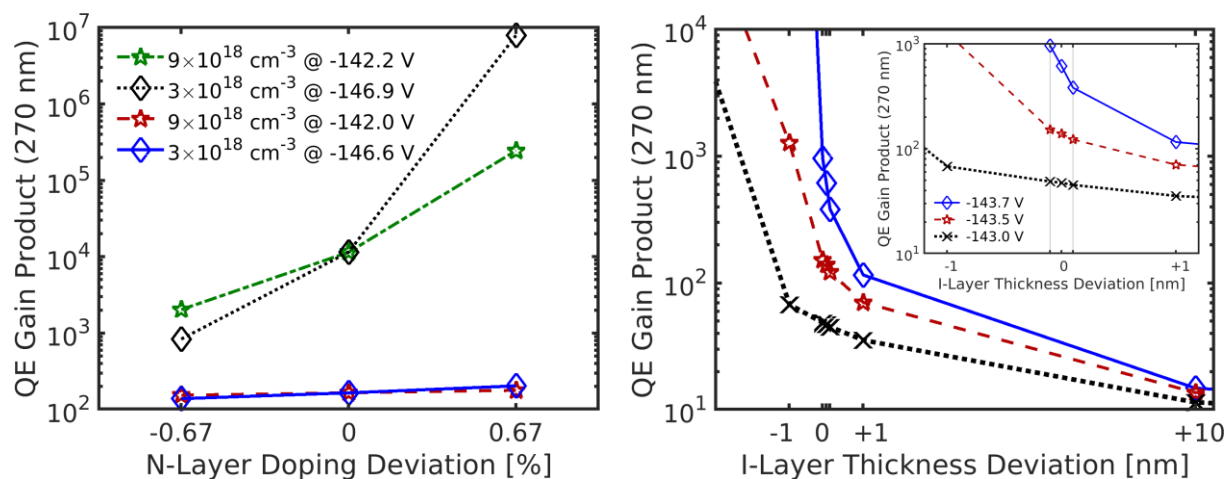


Figure 5: Numerical simulations plotting the QE Gain product due to variations in field-stop layer doping (left) and ML thickness (right) for several applied bias. Inset (right) are the results for i-layer thickness deviation of ± 0.1 nm.

Interestingly, these results suggest that this device exhibits similar behavior to those reported by both Guo *et al.* [15] and Cai *et al.* [14], and that the spatial uniformity is significantly affected by the applied bias. We observed similar behavior in both n-illuminated SiC APDs and SACM structures (detailed results not reported here). Furthermore, spatial-uniformity studies made in linear mode can be indicative of Geiger-mode performance with comparable bias.

To explore the impact of device geometry on the non-uniform response of these APDs, spatial maps of the photoresponse for an n-illuminated SACM structure with three different geometries, all fabricated on the same chip, were investigated, as shown in Figure 4. The device geometries consist of rectangular diodes with sizes $60 \mu\text{m} \times 60 \mu\text{m}$, $90 \mu\text{m} \times 90 \mu\text{m}$, and $30 \mu\text{m} \times 120 \mu\text{m}$. Bias conditions were chosen to minimize the variation in peak gain in these devices ($M = 9000$ to 15000), and to facilitate comparison the measured photocurrent was normalized to the peak current. As shown in Figure 4, the spatial non-uniformity of the response is highly directional, with significantly less variation observed along the horizontal direction than the vertical direction. Specifically, the $30 \mu\text{m} \times 120 \mu\text{m}$ device is the most uniform. It exhibits no optically dead zone, approximately 50% variation in the photocurrent in the vertical direction, and only slight variation in the horizontal direction. In contrast, both the $60 \mu\text{m} \times 60 \mu\text{m}$ and $90 \mu\text{m} \times 90 \mu\text{m}$ devices exhibit optically dead zones across $30 \mu\text{m}$ to $50 \mu\text{m}$ in the vertical direction.

4. MODELING RESULTS

Currently, SiC epitaxial wafer foundries specify layer thickness and doping concentration variations of 6% to 10% over a 100 mm wafer, and $< 25\%$ over a 150 mm wafer. This wide range is associated with variability arising from dopant type (n- or p-) and layer thickness. Assuming that these variations are a gradient across the wafer associated due to the growth-reactor geometry, they may account for differences in behavior between one side of a mesa and the other. However, as the spatial non-uniformity arises on the scale of a $60 \mu\text{m}$ device, the variations in doping and thickness are a factor of $\approx 1000\times$ smaller. To study the effect of these variations on response uniformity, we developed numerical models of several p-i-n 4H-SiC avalanche photodiodes in which the doping in the n- and p- regions, and the thickness of the i- layer, were varied.

Two-dimensional (2D) numerical simulations were performed using Synopsys TCAD Sentaurus [16,17] in which the finite element method is implemented to self-consistently solve the drift-diffusion and Poisson equations, yielding, among other quantities, the photocurrent. Transmission through the anti-reflection coating was calculated externally using a layered thin-film transmission- and reflection-coefficient calculator, using the optical constants for each material, and used to scale the simulated QE during post-processing. For the 4H-SiC bandgap, dielectric constant, and mobility the values from Kimoto have been used [18]. Included in the simulations are Auger, radiative, and Shockley-Reed-Hall (SRH) recombination, where SRH is the limiting recombination mechanism. The SRH model was calibrated to using the

measured quantum efficiency of a SiC PIN diode with structure like that of Liu *et al.* [6]. The electron and hole lifetimes govern the transport from the p- and n-layers respectively. The published values by Liaugaudas *et al.* [19] are used for minority electron lifetime in heavily doped layers. The minority hole lifetime was extracted by fitting the spectral response of the p-i-n diode in the near ultraviolet spectrums, whose photons are primarily absorbed by the doped n-layer, which yields a lifetime of 20 ns at a doping of $3 \times 10^{18} \text{ cm}^{-3}$ using a the dopant dependent carrier mobility model by Kimoto *et al.* [20]. The doping dependence of the minority hole lifetime between $1 \times 10^{15} \text{ cm}^{-3}$ and $3 \times 10^{18} \text{ cm}^{-3}$ was determined using the Scharfetter relation and assuming a value of $1 \mu\text{s}$ at a doping of $1 \times 10^{15} \text{ cm}^{-3}$. Impact ionization is included by using the Thornber model, where the coefficients have previously been calibrated to 4H-SiC material [21].

Figure 5 shows the calculated QE gain-product (photocurrent) for a series of p-i-n APDs where the n-layer doping (left) and the i-layer thickness (right) were varied. The plot uses the product of the internal quantum efficiency and the gain, as this is directly proportional to the photocurrent, but more clearly shows gain is the true dependent variable, as the change in internal quantum efficiency is negligible under all the cases considered. Figure 5 left shows the expected variation in photocurrent for small changes in n-layer doping and at various applied biases in a p-i-n APD with a 500 nm thick i-region and n-layer doped at $3 \times 10^{18} \text{ cm}^{-3}$ (diamonds) and $9 \times 10^{18} \text{ cm}^{-3}$ (stars). At lower bias (low gain), small changes in doping ($\pm 0.67\%$) result in a negligible change in the calculated photocurrent, irrespective of the doping level of the n-layer. However, with increasing bias the gain is highly dependent on small changes in doping, as shown by the 2 to 4 orders of magnitude difference in photocurrent predicted for the same variation. It is important to note that this level of variation is approximately comparable to the possible dopant variation if the spread observed at the wafer level (100 mm) is interpolated to the device level (100 μm). Increasing the doping in the n-layer from $3 \times 10^{18} \text{ cm}^{-3}$ to $9 \times 10^{18} \text{ cm}^{-3}$ reduces in the observed variation with bias.

Figure 5 (right) shows the expected variation in photocurrent for small changes in i-layer thickness and at various applied biases in a p-i-n APD with the n- and p- layers doped at 3×10^{18} and 1×10^{19} , respectively, and a nominal i-region thickness of 500 nm. At the lowest bias examined, a $\pm 0.1 \text{ nm}$ change in i-layer thickness has negligible effect on the calculated photocurrent, while a 10 nm change results in an order of magnitude variation. However, as with the case for doping, the impact of the very small $\pm 0.1 \text{ nm}$ change in i-layer thickness on the photocurrent increases dramatically with increasing gain of the diode. It is evident that even at relatively low gains of <1000 (solid blue lines), minor variations in layer thickness effect the gain by approximately half an order of magnitude, which qualitatively similar trends measured in real devices. Here it is important to note that a $\pm 0.1 \text{ nm}$ variation in i-layer thickness over a device is comparable to the variation if the spread observed at the wafer level (100 mm) is extrapolated to the device level (100 μm).

In all the cases we examined, the large change in photocurrent with the varied parameter is attributed to significant changes in the gain due to changes in the electric field. Both the small changes in doping and thickness result in a change in the depletion width of the structure at a given bias. At low bias, and therefore lower internal electric field, variations have little effect on impact ionization, and hence gain. However, the impact ionization process has an exponential behavior, and as the overall magnitude of the electric field increases these small changes can yield significant changes in gain. This trend agrees well with the experimental data at low gain from the p-i-n and SACM SiC APDs examined in this paper, as well as the work of Guo *et al.* [15]. However, these numerical results do not explain the reduction in non-uniformity at high gain. We note that gain-saturation effects with increasing bias have been observed in other material [22] and attributed

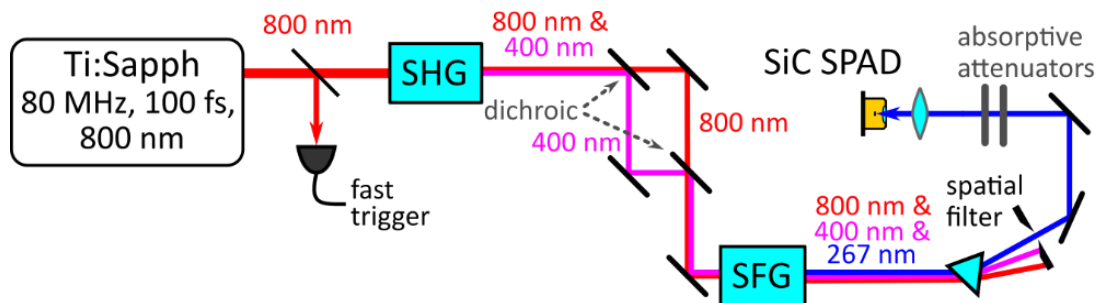


Figure 6. System to characterize the SiC SPAD's temporal resolution at 267 nm. A frequency-tripled Ti:Sapph laser produces $< 100 \text{ fs}$ pulses at 267 nm that are attenuated as focused onto the SPAD. Separation of the SFG pump beams is used to confirm that multi-photon absorption is not contributing to the detector's response, and a dispersive prism is used to spatially separate the 267 nm beam.

to acoustic phonon emission at high energy, and this could be a possible mechanism by which a device's response could become more uniform as the bias is increased [23]. Increasing the overall thickness of i-region, where avalanche multiplication occurs, or the doping in both the p- and n- regions can somewhat mitigate the observed bias-dependent spatial non-uniformity in the device by reducing the variation in depletion width across a device.

5. JITTER RESULTS

There has been little published work on characterizing the temporal resolution of SiC SPADs. To our knowledge, the lowest demonstrated jitter reported in the literature is ≈ 650 ps but this result is a convolution of the ≈ 400 ps UV source used to illuminate the SPAD, as well as contributions from the detector and readout electronics [14]. To minimize the contribution of the UV source and make a more direct characterization of a SiC SPAD's temporal resolution, the femtosecond UV source illustrated in Figure 6 was developed, in which an 80 MHz mode-locked Ti:Sapph laser producing ≈ 100 fs pulses at 800 nm (red line) is frequency-tripled in a series of second-order nonlinear crystals; the first for second harmonic generation (SHG) of 400 nm light (magenta line), and the second for sum-frequency generation (SFG) of 267 nm light (blue line). Due to the high peak powers of the optical pulses in this system, special effort was made to separate the beams; a dispersive prism followed by a spatial filter (a pinhole) is used to spatially filter the 400 nm and 800 nm beams from the 267 nm beam. Special care was taken to separate and recombine the 400 nm and 800 nm beams using dichroic

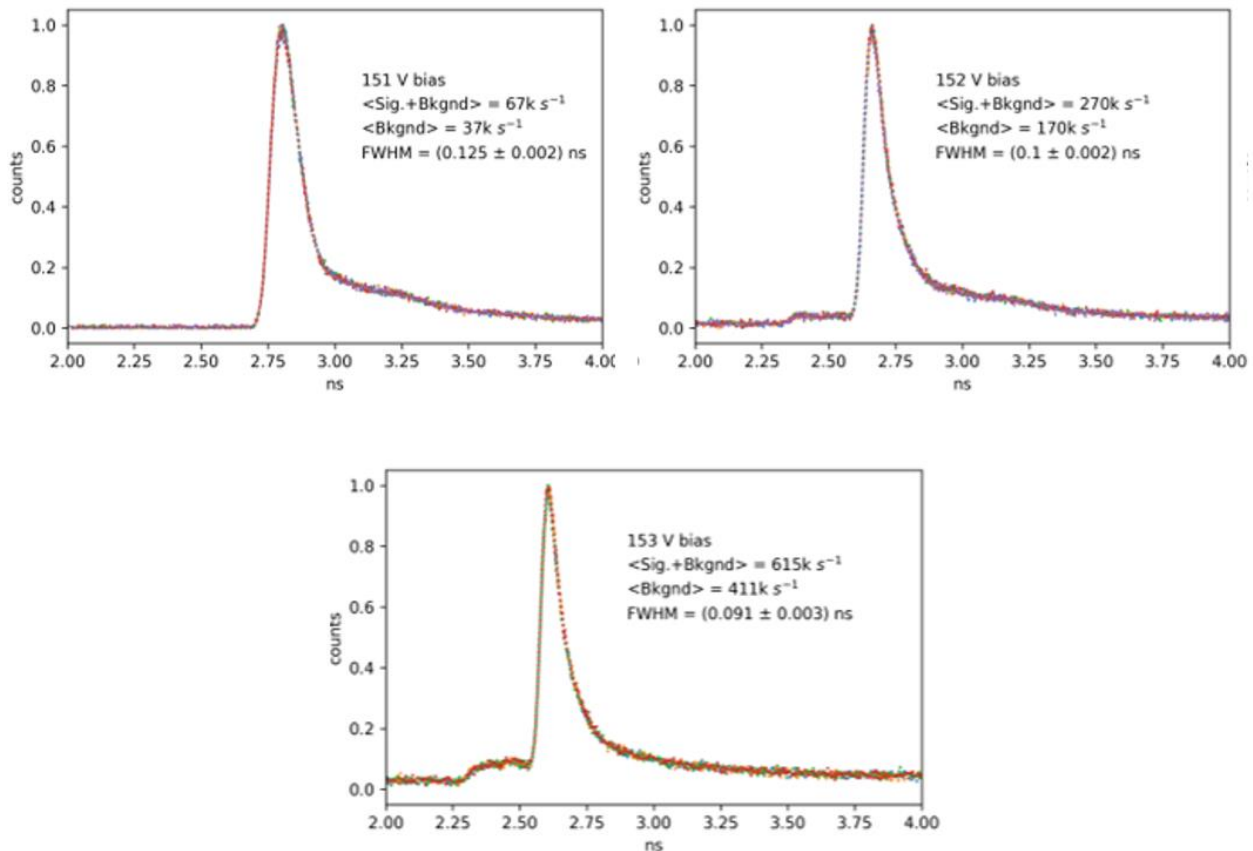


Figure 7. Histograms of detection events when the SiC SPAD is illuminated by attenuated <100 fs 267 nm pulses at 80 MHz. For each operating voltage the following measurement procedure was conducted five times consecutively: we accumulated detection events with the illuminated SPAD until the counts in peak approached ≈ 4000 , then the 267 nm beam was blocked and background detection events were accumulated for the same duration of time and subtracted from the illuminated counts in each bin. In this manner background counts are removed from these histograms. As the voltage is increased, it can be seen that a hump emerges from the noise floor in advance of the main detection peak. We do not know the origin of this effect. The temporal resolution shown here is limited by the passive quenching circuit in which the SPAD is operated.

mirrors between the two nonlinear crystals so that each beam can be blocked independently to confirm that the detector is not responding to any residual or scattered 400 nm or 800 nm photons via multi-photon absorption. Finally, absorptive filters and a 10 cm focal length fused-silica lens attenuate and focus the 267 nm beam onto the SiC SPAD. The SPAD is mounted on a 3-axis micrometer stage (not illustrated) for alignment to the focal spot. The detector's temporal response is very sensitive to the spatial alignment of the focal spot on the detector. We conjecture that this sensitivity correlates with the spatial non-uniformity in the detection efficiency discussed above, though we did not make simultaneous measurements of the DE and temporal resolution. Nonetheless, this understanding agrees with the notion that there are non-uniformities in the electric field across the active region of the device that could degrade both the DE and the jitter.

The detector was biased above breakdown and the attenuation was increased until the count rate of the detector was both well below the laser repetition rate and significantly higher than the background count rate observed with the beam blocked. For example, at a reverse bias of (151 ± 0.5) V and with the 267 nm beam blocked, the background count rate (which includes the dark count rate of the detector and any contribution from stray light) is $37 \times 10^3 \text{ s}^{-1}$, and with the 267 nm beam unblocked we see an overall count rate of $67 \times 10^3 \text{ s}^{-1}$. The temporal response of the SiC SPAD was characterized with a start-stop style time-correlated single-photon counting (TCSPC) system with < 5 ps resolution and a reset time of ≈ 100 ns. The start signal for the TCSPC system is derived from a fast "trigger" photodiode on the 800 nm Ti:Sapph output, as illustrated in Figure 6, and the stop signal is the SPAD's output.

The temporal response at three different reverse bias voltages is shown in Figure 7. The full-width at half-maximum (FWHM) is observed to decrease from ≈ 125 ps to ≈ 91 ps as the reverse bias is increased from 151 V to 153 V. These results are significantly lower than prior reports [12,13] and demonstrate that SiC SPADs can offer high temporal resolution in single-photon-detection applications.

We believe these results to be an upper bound for this device, and that higher temporal resolution may be achievable. As shown in Figure 7, as the excess bias is increased the total count rate (signal plus dark counts) also increases by nearly an order of magnitude, from $67 \times 10^3 \text{ s}^{-1}$ at 151 V, to $615 \times 10^3 \text{ s}^{-1}$ at 153 V, a change which is observed to be dominated by an increase in detector dark counts. This has bearing on the temporal resolution through the passive-quenching circuit in which the device was operated; the 100 k Ω load resistor, in combination with the ≈ 7.4 pF junction capacitance (measured at 151 V reverse bias), means that after each single-photon-detection event the RC time constant for the recovery of the voltage bias on the SPAD is ≈ 0.74 μs and the time to reach 95% of the full excess bias is ≈ 2.2 μs . Thus, with the 80 MHz repetition rate of the laser, as the detector's count rate increases above 10^5 s^{-1} an increasing number of detection events are occurring while the excess bias is still recovering and below its maximal value. This reduces the apparent temporal resolution (and DE) of the detector. It is therefore likely that the ≈ 91 ps FWHM we observe at a reverse bias of ≈ 153 V, where the mean time between detection events is 1.6 μs , is an upper bound. Similarly, the spatial non-uniformity of the detector may also be degrading the jitter of the SPAD when photons are absorbed in a low-field region of the device. We believe that a more spatially uniform device operating in a quenching circuit that actively restores the voltage bias after a detection event (and an appropriate holdoff time) would exhibit temporal resolution better than we report here. Nonetheless, these results are, to our knowledge, the lowest jitter reported for a SiC SPAD, and point towards a path for improvement.

6. SUMMARY

In summary, the jitter and spatial uniformity of the linear-mode and Geiger-mode response of SiC avalanche photodiodes were examined. While the uniformity of the response was observed to be highly directionally dependent, choosing an appropriate device geometry was observed to minimize these effects. Jitter measurements at 267 nm illumination show a FWHM below 92 ps, which is significantly lower than previously reported and potentially an upper-bound due to passive quenching as well as the spatial non-uniformity. While numerical modeling of expected variation in doping and layer thickness across a small area device indicates that it may be potentially responsible for the observed non-uniformity in response, both effects can to some extent be mitigated through device design.

REFERENCES

- [1] Specification sheet for Hamamatsu S13370-xxxxCN Si APDs.
- [2] <https://andor.oxinst.com/products/istar-intensified-cameras>

- [3] <https://thinklucid.com/tech-briefs/sony-4th-generation-pregius-s/>
- [4] Guo, X., Rowland, L.B., Dunne, G.T., Fronhieser, J.A., Sandvik P.M., Beck, A. L., and Campbell, J.C., "Demonstration of ultraviolet separate absorption and multiplication 4H-SiC avalanche photodiodes" *IEEE Phot. Tech. Lett.* **18**, 136 (2006).
- [5] Zhou, X., Han, T., Liu, Y., Li, J., Lu, W., Wang, Y., Song X., Tan, X., Liang, S., Feng, Z., and Cai, S., "Large-area 4H-SiC ultraviolet avalanche photodiodes based on variable-temperature reflow technique" *IEEE Elect. Dev. Lett.* **39**, 1724 (2018).
- [6] Liu, H., McIntosh, D., Bai, X., Pan, H., Liu, M., Campbell, J.C, and Cha, H.Y," 4H-SiC PIN recessed-window avalanche photodiode with high quantum efficiency" *IEEE Phot. Tech. Lett.* **20**, 1551 (2008).
- [7] Vert, A., Soloviev, S., Fronheiser, J., and Sandvik, P., "Solar-blind 4H-SiC single-photon avalanche diode operating in Geiger mode" *IEEE Phot. Tech. Lett.* **20**, 1587 (2008).
- [8] Bai, X.G., Guo, X.Y., McIntosh, D.C., Liu, H.D., and Campbell, J.C., "High detection sensitivity of ultraviolet 4H-SiC avalanche photodiodes" *IEEE J. Quantum Electron.* **43**, 1159 (2007).
- [9] X. Bai, H. D. Liu, D. C. McIntosh, and J. C. Campbell, "High-detectivity and high-single-photon-detection-efficiency 4H-SiC avalanche photodiodes" *IEEE J. Quantum Electron.* **45**, 300 (2009).
- [10] Zhou, D., Liu, F., Lu, H., Chen, D., Ren, F., Zhang, R., and Zheng, Y., "High-temperature single photon detection performance of 4H-SiC avalanche photodiodes" *IEEE Phot. Tech. Lett.* **26**, 1136, (2014).
- [11] Soloviev, S., Dolinsky, S., Palit, S., Zhu, X., and Sandvik, P., "Silicon Carbide solid-state photomultiplier for UV light detection," *Sensors for Extreme Harsh Environments*, Proc. of SPIE vol. 9113, pp. 9111305, 2014
- [12] Bai, X., McIntosh, D., Liu, H., and Campbell, J.C, "Ultraviolet Single Photon Detection With Geiger-Mode 4H-SiC Avalanche Photodiodes," *IEEE Photon Tech. Lett.* **19**, 1822 (2007).
- [13] Soloviev, S., Vert, A., Bolotnikov, A. and Sandvik, P., "UV SiC avalanche photodetectors for photon counting" *Sensors*, 1897 (2009).
- [14] Cai X, Wu C, Lu H, et al. Single photon counting spatial uniformity of 4H-SiC APD characterized by SNOM-based mapping system. *IEEE Photon Tech Lett*, **29**, 1603 (2017).
- [15] Guo, X., Beck, A. L., Li, X., Campbell, J. C., Emerson, D., and Sumakeris, J., "Study of reverse dark current in 4H-SiC avalanche photodiodes" *IEEE Journal of quantum electronics*, **41**, 562-567, (2005).
- [16] The identification of any commercial product or trade name does not imply endorsement or recommendation by the National Institute of Standards and Technology.
- [17] Synopsys, Sentaurus Device User Guide (2021). Version S-2021.06.
- [18] Kimoto, T. and Cooper, J. A., *Physical Properties of Silicon Carbide*. John Wiley & Sons, Ltd, 2014, ch. 2, pp. 11–38. [Online]. Available: <https://onlinelibrary.wiley.com/doi/abs/10.1002/9781118313534.ch2>
- [19] Liaugaudas, G., Dargis, D., Kwasnicki, P., Arvinte, R., Zielinski, M. and Jarašiūnas, K., "Determination of carrier lifetime and diffusion length in Al-doped 4H-SiC epilayers by time-resolved optical techniques," *J. Phys. D: Appl. Phys.*, Vol. 48, pp. 025103 (2015)
- [20] Kimoto T., and Cooper J., "Fundamentals of Silicon Carbide Technology: Growth, Characterization, Devices, and Applications" First Edition, Wiley-IEEE Press, ISBN: 978-1-118-31352-7 (2014) Pages 23-24,522-523
- [21] Nouketcha, F. L. L., Cui, Y., Lelis, A., Green, R., Darmody, C., Schuster, J., and Goldsman, N., "Investigation of wide- and ultrawide-bandgap semiconductors from impact-ionization coefficients," *IEEE Trans. Electron Devices.* **67**(10), pp. 3999–4005 (2020).
- [22] Rothman, J., Mollard, L., Bosson, S., Vojetta, G., Foubert, K., Gatti, S., Bonnouvrier, G., Salveti, F., Kerlain, A. and Pacaud, O., *J. Electron. Mater.*, Vol., "Short-wave infrared HgCdTe avalanche photodiodes" *Journal of electronic materials*, **41**, 2928-2936 (2012).
- [23] Bertazzi, F., Moresco, M., Penna, M., Goano, M. and Bellotti, E., "Full-band Monte Carlo simulation of HgCdTe APDs" *Journal of Electronic Materials*, **39**, 912-917, (2010).